Characterization of condensation on nanostructured surfaces and associated thermal hydraulics using a thermal lattice Boltzmann method

Aritra Mukherjee,[1,*] Dipankar N. Basu,[1,2,†] Pranab K. Mondal,[1,‡] and Lin Chen[2,3,§]
[1]*Department of Mechanical Engineering, Indian Institute of Technology Guwahati, Guwahati 781039, India*
[2]*Institute of Engineering Thermophysics, Chinese Academy of Sciences, Beijing 100190, China*
[3]*University of Chinese Academy of Sciences, Beijing 100049, China*

(Received 14 January 2022; accepted 24 March 2022; published 13 April 2022)

The dynamics of the condensation process on nanostructured surfaces can be modulated substantially by tuning the surface architecture. Present study uses the mesoscopic framework of lattice Boltzmann method (LBM) to explore the role of surface morphology and cold spot temperature in determining the visual state of the condensate droplet, mode of nucleation, and associated rates of energy and mass interactions. A multiple relaxation time–(MRT)-based LBM solver, coupled with pseudopotential model, has been developed to simulate a rectangular domain of saturated vapor, housing a cold spot on the bottom rough surface. Superhydrophobicity has been achieved for certain combinations of surface parameters, with the intercolumn spacing being the most influential one. Gradual increase in the spacing modifies the nucleation mode from top through side to bottom, while the droplet changes from Cassie to Wenzel state. The Cassie drop in top nucleation mode exhibits the largest contact angle and least rate of surface heat transfer. Both types of Wenzel drops display large rate of condensation and two peaks in heat transfer, along with very short nucleation time in comparison with Cassie drops. Couple of phase diagrams have been developed combining all four scenarios of condensation predicted by the present model. One important novelty of the present study is the consideration of nonisothermal condition within LB structure. Enhancement in the degree of subcooling at the cold spot encourages greater condensation and Cassie-to-Wenzel transition.

DOI: 10.1103/PhysRevE.105.045308

I. INTRODUCTION

The thermalhydraulics of the process of condensation regulates several of our everyday experiences, such as dew and frost formation, hydrologic cycle, and fogging of eyeglasses or mirrors. The inherent physics can be quite similar to its counterpart in evaporation, with droplet nucleation from saturated or subcooled vapor, gradually growing into a condensate drop with time [1,2]. However, there are also noticeable differences, with enhanced role of the surface morphology and. substantially higher level of heat transfer coefficient, especially while dealing with heterogeneous nucleation [1,3], which is more prevalent in nature owing to the requirement of lower activation energy in comparison to the homogeneous version. Heterogeneous condensation also plays pivotal role in numerous industrial and commercial appliances, liquid distillation, solar desalination, power cycles, refrigerators and air-conditioners, and cleaning of exhaust gases, to name a few. Consequently, vapor condensation on solid substrate has always been a fascinating domain of research to both theoreticians and experimentalists [4–8].

Superhydrophobic surfaces with micro- or nanostructures have attracted considerable attention in recent years within both the scientific and industrial communities because of their distinct wetting characteristics and various alluring features such as,. heat transfer enhancement, quick droplet removal, self-cleaning, and defrosting [9–12]. The architecture of such structured surfaces significantly influences the nature of droplet nucleation and growth pattern, subsequently amending the extent of interfacial interactions. A condensate droplet evolving on a solid surface can unveil two different nucleation patterns depending on the roughness topology of the surface itself, namely the Wenzel state and Cassie state. As shown in Fig. 1, the former refers to the situation with the droplet propagating inside the grooves formed by the microcolumns and wetting the entire solid surface. In the Cassie state, however, the droplet sits on top of the columns and does not conform to the actual base. Following Quéré [13], roughness can be viewed to alter the apparent wettability of the solid, and consequent water repellency, owing to the unbalanced Laplace pressure, which, in turn, is dependent on the curvature of the meniscus inside and outside the grooves. When the Laplace pressure below the interface is lower, the droplet is drawn to the interface, conceiving the Wenzel state, while the reverse entices it toward the tip for the Cassie state. If the liquid droplet attains Cassie state with an apparent contact angle larger than 150° and roll-off angle less than 10°, then the surface can be earmarked as a superhydrophobic one, which has immense potential in several industries. An

*m.aritra@iitg.ac.in
†dnbasu@iitg.ac.in
‡pranabm@iitg.ac.in
§chenlin2018@iet.cn

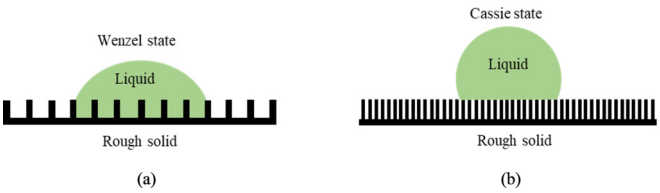

FIG. 1. Pictorial representation of the Wenzel and Cassie states of the condensate droplet in a solid surface with micro- or nanostrcutures.

ordinary hydrophobic surface ornamented with carefully designed nanostructures may exhibit superhydrophobicity [14], which makes the thorough recognition of the influence of surface topology on the droplet condensation characteristics a must for optimized constitution of the solid substrate, as that will help exercising control over the entire process in industrial applications. Several research groups have, therefore, steered their recent endeavor on conception of droplet nucleation on rough surfaces using experimental techniques [15–20], which have asserted the possibility of roughness-induced superhydrophobicity. While the meticulous appraisal of the experimental observations have successfully unearthed critical information about the visual nature of the nucleation process and gross transport attributes, use of multidimensional computational tools are essential to ascertain the local thermohydrodynamic information, and a comprehensive review of the same is available in Enright *et al.* [21].

Lattice Boltzmann method (LBM) has emerged as an excellent alternative to the conventional computational methods [22] in the present millennium, particularly for simulation of multiphase scenarios, owing to its numerous advantageous features, such as lower computational cost, easier implementation and amenability to parallelization. First instance of employing LBM to study condensation of a single drop and its movement on a vertical hydrophobic flat plate can probably be credited to Liu and Cheng [23], which was followed by quite a few other efforts to ascertain condensation on smooth surface structured with various surface wettability patterns [24–27]. Similar efforts toward condensation on a rough surface with micro- or nanostructures, however, are rather limited. Both Zhang *et al.* [14] and Fu *et al.* [28] explored isothermal droplet condensation on superhydrophobic nanoarrays and demonstrated the possibility of appearance of both nucleation states depending on the topology of the substrate. Li *et al.* [29] delved into the growth of the Cassie and Wenzel droplets on a rough surface with variable wettability and fixed roughness in a gravity-free environment, whereas solely the nucleation and growth patterns, without discriminating between the states or wetting behavior, were investigated by Vasyliv *et al.* [30]. Montessori *et al.* [31] introduced an additional force term to simulate near-contact repulsive forces between nonsimilar droplets in a multicomponent isothermal environment. Recent effort of integrating multiparticle collision dynamics in LB framework [32,33], for improved resolution of molecular forces, can also be noted, though that is still a work in progress. The pseudopotential-based entropic LB model of Montessori *et al.* [34] has also shown encouraging performance in replicating droplet dynamics at the absence of external heat transfer.

To the best of our knowledge, none of the published literature interrogated the combined effect of the roughness topology and surface temperature on the condensation process on a nanostructured rough surface, specifically for a temperature-controlled system. While the finite-volume-based methods require the assumption of an initial interface, thereby limiting their competence, available LB models are generally isothermal in nature. To address the same, we focus on envisaging the impact of the architecture of the solid substrate in determining the Cassie or Wenzel state, and subsequent behavior adhering to the mesoscopic framework of LBM. Our study encompasses several combinations of the surface morphology and cold spot temperature on a horizontal rough surface, with the droplet growth pattern, condensate mass accumulation rate, heat transfer rate and nucleation time being the variables considered for subsequent analyses, as our primary aspiration is the comprehension of the surface conditions leading toward superhydrophobicity. Successful completion of the present study will help us in concluding about the specifications of the micro- or nanocolumns desirable to attain a specific droplet state. Consideration of the nonisothermal media is a major novelty of the present study, while it also methodically dissects each of the dimensions of the nanoarray, thereby allowing us to apprise their respective importance.

We can present here a brief rundown of the manuscript organization. Section II describes the mathematical framework of the employed multiphase LBM version, whereas the output of the same have been analyzed in Sec. III. Finally, we summarize the major conclusions in Sec. IV.

II. MATHEMATICAL FORMULATION

We have employed the multiple relaxation time–(MRT) based LBM framework in the present study, with the Shan-Chen (SC) pseudopotential model to emulate phase-change process in a nonisothermal medium. As per the LB philosophy, the local instantaneous population density at the lattice level is modeled in terms of the particle distribution function (PDF) $f(\mathbf{x}, \boldsymbol{\zeta}, t)$, whereas the energy distribution function $g(\mathbf{x}, \boldsymbol{\zeta}, t)$ corresponds to the lattice-level temperature in a double-distribution function (DDF) approach. Here $\mathbf{x}$ and t respectively refer to the lattice position and time instant under consideration, whereas $\boldsymbol{\zeta}$ comprises of the discrete set of lattice-level velocities.

A. Conservation of linear momentum

The evolution of fluid motion at the lattice level is simulated by the transformation of the probabilistic distribution of PDFs in both physical and velocity space. The classical Shan-Chen formulation employs the BGK collision operator based on single relaxation time [35]. It is, however, a recent observation that the use of multiple relaxation time to cater the different directions of PDF dissemination can lead to enhanced numerical stability and accuracy, which has inspired the adoption of MRT-based SCLBM [36,37] in the present work. Here we need to transform the population from the velocity space to the moment space using a transformation matrix $[M]$ to execute the collision step

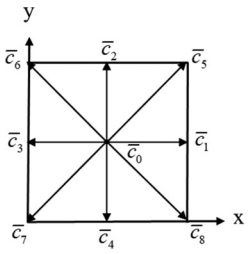

i	w_i	c_i
0	$4/9$	(0,0)
1-4	$1/9$	(±1,0),(0,±1)
5-8	$1/36$	(±1,±1)

FIG. 2. Vectorial representation of the D2Q9 lattice adopted in the present study, with associated information.

and then transfer back the post-collision set using $[M]^{-1}$ for streaming. Consequently, the collision equation governing the conservation of momentum at the mesoscopic level can be expressed as

$$f_i(\mathbf{x}+\mathbf{c}_i\Delta t, t+\Delta t) = f_i(\mathbf{x},t) - M^{-1}S_f M\left(f_i - f_i^{\mathrm{eq}}\right)\Delta t + F_i(\mathbf{x},t)\Delta t, \quad (1)$$

where f_i is the PDF with lattice-level velocity of $\mathbf{c}_i$. The equilibrium magnitude of the PDF f_i^{eq} can be written as

$$f_i^{\mathrm{eq}}(\rho,\mathbf{u}) = w_i\,\rho(\mathbf{x},t)\left[1+\frac{\mathbf{u}\cdot\mathbf{c}_i}{c_s^2}+\frac{(\mathbf{u}\cdot\mathbf{c}_i)^2}{2c_s^4}-\frac{\mathbf{u}\cdot\mathbf{u}}{2c_s^2}\right]. \quad (2)$$

Here w_i and $\mathbf{c}_i$ respectively correspond to the weight factor and lattice velocity in the ith direction and c_s is the speed of sound at the lattice scale. We have restricted our analyses to two dimensions, for which $\mathbf{c}_i = \frac{\Delta x}{\Delta t}\hat{i} + \frac{\Delta y}{\Delta t}\hat{j}$ and $c_s = \mathbf{c}_i/\sqrt{3}$. Complete details about the velocity sets and weights for the selected D2Q9 lattice are available in Fig. 2. ρ and $\mathbf{u}$ are representative of mass density and fluid velocity respectively, and their detailed definitions are available below.

A very important component of Eq. (1) is the orthogonal transformation matrix M, which allows the mutation of the PDFs from the velocity space to the moment space, and it has the following definition for a D2Q9 lattice.

$$M = \begin{bmatrix} 1 & 1 & 1 & 1 & 1 & 1 & 1 & 1 & 1 \\ -4 & -1 & -1 & -1 & -1 & 2 & 2 & 2 & 2 \\ 4 & -2 & -2 & -2 & -2 & 1 & 1 & 1 & 1 \\ 0 & 1 & 0 & -1 & 0 & 1 & -1 & -1 & 1 \\ 0 & -2 & 0 & 2 & 0 & 1 & -1 & -1 & 1 \\ 0 & 0 & 1 & 0 & -1 & 1 & 1 & -1 & -1 \\ 0 & 0 & -2 & 0 & 2 & 1 & 1 & -1 & -1 \\ 0 & 1 & -1 & 1 & -1 & 0 & 0 & 0 & 0 \\ 0 & 0 & 0 & 0 & 0 & 1 & -1 & 1 & -1 \end{bmatrix} \quad (3)$$

The column vector $S_f = (\tau_0^f\ \tau_1^f\ \tau_2^f\ \tau_3^f\ \tau_4^f\ \tau_5^f\ \tau_6^f\ \tau_7^f\ \tau_8^f)^T$ contains the relaxation times in the moment space, where the final two are related to the kinematic viscosity (ν) of the fluid as $\tau_7^f = \tau_8^f = 3\nu + 0.5$, and the others are adjustable and selected based on the relevant literature.

Equation (1) is often simplified by introducing the following combination:

$$m^* = m - S_f(m - m_{\mathrm{eq}})\Delta t + M\mathbf{F}\Delta t, \quad (4)$$

where $m = Mf$ and $m_{\mathrm{eq}} = Mf_{\mathrm{eq}}$. The last term on the right-hand side can further be expanded by introducing a forcing term $\bar{S}$ as $M\mathbf{F} = (I - \frac{S_f}{2})\bar{S}$, with I being the unit tensor, for ease of analysis in the moment space. Accordingly, Eq. (1) evolves to yield the population for the next time step as

$$f_i(\mathbf{x}+\mathbf{c}_i\Delta t, t+\Delta t) = M^{-1}m_i^*. \quad (5)$$

The lattice-level mass density can be computed from the zeroth moment of the PDF as

$$\rho(\mathbf{x},t) = \sum_i f_i(\mathbf{x},t). \quad (6)$$

Estimation of the fluid velocity, however, requires a knowledge about the prevailing body force field, as it is defined as,

$$\mathbf{u}(\mathbf{x},t) = \sum_i f_i(\mathbf{x},t)\mathbf{c}_i + \frac{\mathbf{F}\Delta t}{2\rho}, \quad (7)$$

with $\mathbf{F}$ being the total force acting on the body. The estimation involves use of the forcing term $\bar{S}$ defined earlier in the moment space, and it can be expressed as [38]

$$\bar{S} = \begin{bmatrix} 0 \\ 6(u_xF_x + u_yF_y) + \frac{\sigma_m|\mathbf{F}^{\mathrm{SC}}|^2}{\psi^2\Delta t(\tau_7-\frac{1}{2})} \\ -6(u_xF_x + u_yF_y) - \frac{\sigma_m|\mathbf{F}^{\mathrm{SC}}|^2}{\psi^2\Delta t(\tau_7-\frac{1}{2})} \\ F_x \\ -F_x \\ F_y \\ -F_y \\ 2(u_xF_x - u_yF_y) \\ u_xF_y + u_yF_x \end{bmatrix}, \quad (8)$$

where σ_m is a parameter able to tune the stability of simulation and a choice of $\sigma_m = 0.103$ has helped us achieve the best results in the present work.

The body force relevant to a condensation problem comprises of the interparticle interaction force or the so-called Shan-Chen force ($\mathbf{F}^{\mathrm{SC}}$), the surface wettability force ($\mathbf{F}^{w}$), and the external force ($\mathbf{F}^{\mathrm{ext}}$). Here the last one is the representative of all possible external force field. Gravity is the only one contemplated with in the present work and that has been estimated following Liu and Cheng [24] as

$$\mathbf{F}_i^{\mathrm{ext}}(\mathbf{x},t) = \mathbf{g}_a[\rho(\mathbf{x},t) - \rho_{\mathrm{vap}}(t)], \quad (9)$$

with $\rho_{\mathrm{avg}}(t)$ being the instantaneous density of the fluid averaged over the entire computational domain under consideration and $\mathbf{g}_a$ being the lattice-level gravitational acceleration.

B. The pseudopotential model

Shan and Chen [39] introduced a pseudopotential function to estimate the interparticle interaction force $\mathbf{F}^{\mathrm{SC}}$, which had

the following original form:

$$\mathbf{F}^{\mathrm{SC}}(\mathbf{x},t) = -G\psi(\mathbf{x},t)\sum_i w_i(|\mathbf{c}_i|)\psi(\mathbf{x}+\mathbf{c}_i\Delta t,t)\mathbf{c}_i\Delta t. \tag{10}$$

Here $\psi(\mathbf{x},t)$ is referred as the pseudopotential function and it is reliant on the local lattice-node density. For the adopted D2Q9 lattice,

$$w_i(|\mathbf{c}_i|) = \begin{cases} w_1 & \text{if } |\mathbf{c}_i| = \mathbf{c}_i \\ w_2 & \text{if } |\mathbf{c}_i| = \sqrt{2}\mathbf{c}_i \\ 0 & \text{otherwise} \end{cases}, \tag{11}$$

with the constraints of $w_1 = 4w_2$, originating from the weight factors associated with the velocity distribution of a D2Q9 lattice, as detailed in Fig. 2, and $G(\mathbf{x},\tilde{\mathbf{x}}) = w_i G$ for $\tilde{\mathbf{x}} = \mathbf{x} + \mathbf{c}_i\Delta t$ and zero otherwise.

One of the principle advantages of the SCLBM multiphase model is the attainment of the natural phase separation, without necessitating the assumption of any initial interface unlike conventional CFD tools, which can be realized through a nonideal-gas equation of state (EOS). If the SC pseudopotential force is expanded following Taylor series, while imposing the constraints of the symmetry of the velocity set, then we get the continuum form of the same as

$$\mathbf{F}^{\mathrm{SC}}(\mathbf{x},t) = -G\psi(\mathbf{x},t)\big\{c_s^2\Delta t^2\nabla\psi(\mathbf{x},t) + \tfrac{1}{2}c_s^4\Delta t^4\nabla[\nabla\psi(\mathbf{x},t)]\big\}. \tag{12}$$

The Shan-Chen EOS (SC-EOS) can now be obtained by comparing the first term on the right-hand side with the anisotropic pressure tensor of the macroscopic momentum equation valid for multiphase flow [40]. Accordingly, the nonideal SC-EOS can be written as

$$p(\rho) = c_s^2\rho + \tfrac{1}{2}Gc_s^2\Delta t^2\psi^2(\rho). \tag{13}$$

An important constraint on the EOS is the physical requirement of having coexistence of phases at the saturated condition, which involves a complex interdependency of pressure, temperature, and phase densities. For a given combination of pressure and temperature, the densities of both the phases, with which they can coexist, can be determined from the Maxwell area construction rule [41]. One major issue with the SC-EOS [Eq. (13)] is the explicit absence of temperature, which denies us to retrieve the densities of individual phases, leading to the nonadherence to the coexistence curve and a thermodynamically inconsistent model.

Yuan and Schaefer [41] suggested an alternate way of incorporating realistic EOS by separating the pseudopotential from Eq. (13) as

$$\psi(\mathbf{x}) = \sqrt{\frac{2\big(p - c_s^2\rho\big)}{c_s^2\Delta t^2|G|}}. \tag{14}$$

Now p can be replaced here by a reliable EOS, capable to accurately replicate the liquid-vapor phase-change process. We have used the Peng-Robinson EOS (PR-EOS), which can be seen as the most accurate cubic equation to estimate the liquid and vapor densities interior to the vapor dome [42]. It can expressed as

$$p(\mathbf{x},t) = \frac{\rho RT}{1-b\rho} - \frac{a\alpha(T)\rho^2}{1+2b\rho-b^2\rho^2}, \tag{15}$$

where

$$\alpha(T) = 1+\kappa\big(1-\sqrt{T/T_c^2}\big)^2$$
$$\kappa = 0.37464 + 1.54226\omega - 0.26992\omega^2$$
$$a = 0.45724(R^2T_c^2/p_c) \quad b = 0.0778(RT_c/p_c).$$

Here ω is known as the ascentric factor, the magnitude of which is dependent on the choice of fluid. We have selected R134a as the working fluid in the present study, for which the constants a and b have values of 249 and 221, respectively [41], after setting the lattice-level magnitude of the universal gas constant as 1. In order to maintain the consonance between the macroscopic and mesoscopic scales, the principle of corresponding states must be adhered with, which demands the reduced magnitudes of variables to be identical at both scales. Consequently,

$$\rho_R = \frac{\rho^{\mathrm{LB}}}{\rho_c^{\mathrm{LB}}} = \frac{\rho^{\mathrm{real}}}{\rho_c^{\mathrm{real}}}, \quad p_R = \frac{p^{\mathrm{LB}}}{p_c^{\mathrm{LB}}} = \frac{p^{\mathrm{real}}}{p_c^{\mathrm{real}}},$$
$$T_R = \frac{T^{\mathrm{LB}}}{T_c^{\mathrm{LB}}} = \frac{T^{\mathrm{real}}}{T_c^{\mathrm{real}}}. \tag{16}$$

The above set of relations allows us to impose any specific operating conditions at the lattice level, using the real-life knowledge and also upscale the predicted mesoscale results to macroscale.

The discussions of Yuan and Schaefer [41] help us surmise that the use of realistic EOS instead of traditional SC-EOS can render thermodynamic consistency in the SCLBM formulation over a certain temperature range, within which coexisting densities at a certain temperature dovetail well with the analytical values obtained from the Maxwell area construction rule. With PR-EOS in SRT structure, they found the values to veer for temperature lower than $T_R = 0.9$. It is expected to improve with the adoption of MRT, which is numerically more stable, and we shall explore that in the later part of this study.

The surface wettability force $\mathbf{F}^w$ can also be calculated using the pseudopotential function. A simple model was proposed by Benzi *et al.* [43] to counter the interaction of a single-component multiphase flow with a solid wall, where the desired contact angle, and hence the requisite value of surface tension, can be realized through the so-called false wall density ρ_w [22], which can be envisaged as the density of the fluid at the location of the wall. Accordingly,

$$\mathbf{F}^w(\mathbf{x},t) = -G\psi(\mathbf{x},t)\sum_i w_i\psi(\rho_w)S_{\mathrm{ind}}(\mathbf{x}+\mathbf{c}_i\Delta t)\mathbf{c}_i\Delta t, \tag{17}$$

where the indicator function S_{ind} designates solid or fluid phase by respectively attaining values of one and zero, thereby facilitating the estimation of $\mathbf{F}^w$ only at the wall.

C. Conservation of energy

A second distribution function is necessary to construe the temperature field as per the DDF approach. Continuing

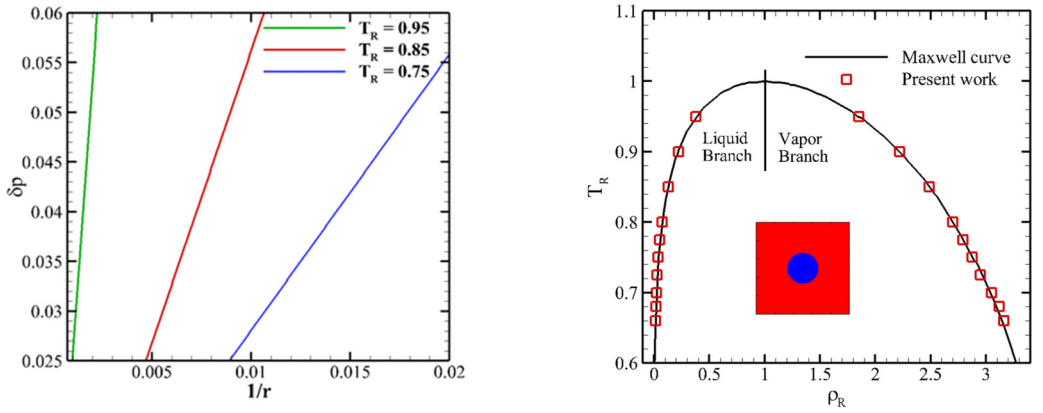

FIG. 3. (a) Laplace test: Inverse of the radius $(1/r)$ of the static droplet (shown in inset) shows a linear relationship with pressure differential across the interface $(\delta p = p_{\text{in}} - p_{\text{out}})$ for three different T_R values. (b) Maxwell area construction rule: excellent conformity between the analytical and numerical coexisting density values for both the phases even for $T_R < 0.7$.

with MRT-LBM to ensure superior numerical stability and solution accuracy, the corresponding governing equation can be written as

$$g_i(\mathbf{x} + \mathbf{c}_i\Delta t, t + \Delta t) = g_i(\mathbf{x}, t) - M^{-1}S_g M\left(g_i - g_i^{\text{eq}}\right) + \delta_t\omega_t\Phi_c(\mathbf{x}, t), \quad (18)$$

with the transformation matrix M being the same as used earlier in Eq. (3). The relaxation times associated with the energy equation constitute the column vector S_g precisely the way S_f has been defined earlier for the momentum conservation equation [37], where τ_3^g and τ_5^g are related to the mesoscopic thermal diffusivity of the concerned fluid as $\tau_3^g = \tau_5^g = 3\alpha + 0.5$.

The equilibrium profile of the energy distribution function is considered as

$$g_i^{\text{eq}}(\rho, \mathbf{u}, T) = w_i T(\mathbf{x}, t)\left[1 + \frac{\mathbf{u}\cdot\mathbf{c}_i}{c_s^2} + \frac{(\mathbf{u}\cdot\mathbf{c}_i)^2}{2c_s^4} - \frac{\mathbf{u}\cdot\mathbf{u}}{2c_s^2}\right] \quad (19)$$

with the lattice-level nodal temperature being defined as the zeroth moment as $T(\mathbf{x}, t) = \sum_i g_i(\mathbf{x}, t)$. Φ_c is the lattice-level latent energy source or sink term associated with the condensation heat transfer process explored here, which can be estimated by combining the Clapeyron equation with the conservation of mass [44] as

$$\Phi_c(\mathbf{x}, t) = T\left[1 - \frac{1}{\rho c_v}\left(\frac{\partial p}{\partial T}\right)_\rho\right]\nabla\cdot\mathbf{u}. \quad (20)$$

We have used second-order central difference scheme to compute the divergence of velocity, while $(\frac{\partial p}{\partial T})_\rho$ can directly be obtained from the adopted PR-EOS. SC-LBM being a diffused-interface approach, it may become necessary to estimate the relevant fluid properties at the interface as the weighted-average one. For any representative thermophysical property γ, the same can be expressed as

$$\gamma = \gamma_{\text{liq}}\frac{\rho - \rho_{\text{vap}}}{\rho_{\text{liq}} - \rho_{\text{vap}}} + \gamma_{\text{vap}}\frac{\rho_{\text{liq}} - \rho}{\rho_{\text{liq}} - \rho_{\text{vap}}}. \quad (21)$$

III. RESULTS AND DISCUSSION

The primary objective of the present study is the exploration of the effect of the morphology of the solid substrate and its degree of subcooling on the mode of droplet nucleation and subsequent development, which can be characterized in terms of the mass condensation rate, nucleation time, and the associated rate of heat transfer. To accomplish the same, an in-house MRT-SC-LBM code has been developed to simulate condensation on rough surfaces following the mathematical structure detailed in Sec. II. It is imperative to validate the code for both isothermal and nonisothermal situations to reap confidence on its correctness, and the same is presented in the following two subsections.

A. Model validation: Laplace test and Maxwell area construction curve

The process of phase separation being spontaneous in the framework of the pseudopotential-based LBM, there is no need of adopting additional interface tracking algorithm. The Laplace test is a very popular practice followed within the LB community to assess the accuracy of interface generation by following the variation of the inverse droplet radius $(1/r)$ with pressure differential across the interface $(\delta p = p_{\text{in}} - p_{\text{out}})$ for a specific temperature. According to Laplace's principle, they must exhibit a linear relationship, with surface tension being the constant of proportionality. Prediction from our numerical model is presented in Fig. 3(a) for $T_R = 0.9$, which aptly demonstrates the successful acquisition of surface tension.

Another indispensable appraisal for any multiphase LBM code is for the predicted magnitudes of the liquid and vapor densities corresponding to the imposed saturation temperature, which must adhere to the analytical levels obtained from the Maxwell area construction rule [41] in order to corroborate the thermodynamic consistency of the numerical structure, as discussed earlier. We have, therefore, performed static droplet test for a wide range of the reduced temperature (T_R), and consequent predictions are available in Fig. 3(b). There is no perceptible difference between the analytical and numerical magnitudes of ρ_R^v and ρ_R^l even when the reduced level

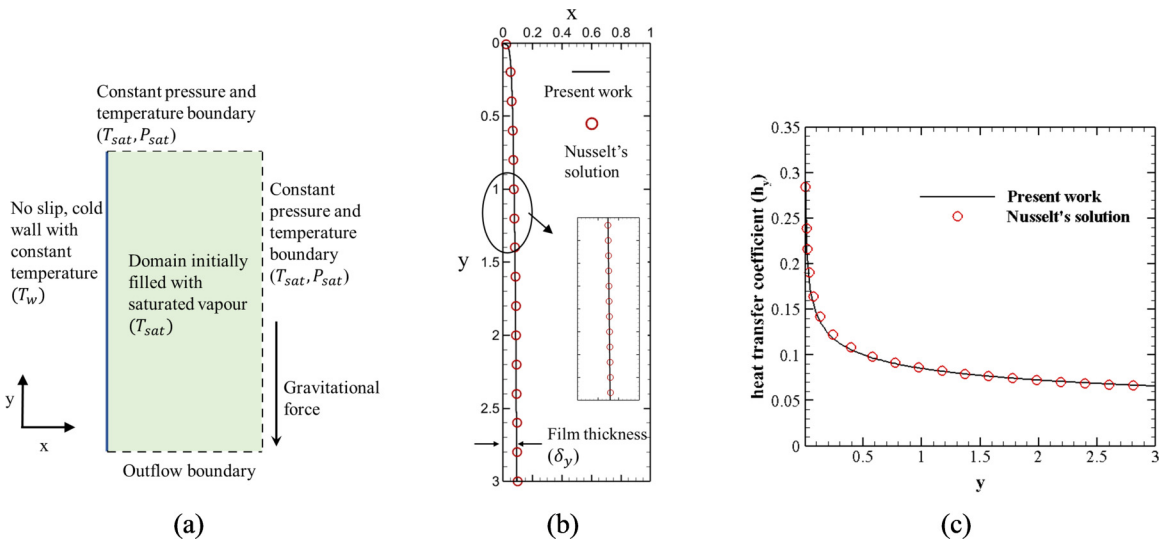

FIG. 4. (a) Schematic representation of the computational domain to analyze condensation on a vertical subcooled wall. Variations in (b) condensate film thickness and (c) local heat transfer coefficient along the surface of the plate and comparison with the Nusselt's analytical solution [2].

of saturation temperature is around 0.65, which sufficiently encompasses the scope of the present study, thereby substantiating the accuracy of the developed computation setup for exploration of multiphase flows.

B. Model validation: Nusselt's falling film

Next we apply the in-house code to simulate the seminal problem of Nusselt's falling film in order to perceive its capability in replicating condensation heat transfer. Here we have a vertical flat plate of temperature T_w maintained in contact with saturated vapor of temperature T_s ($T_s > T_w$). Owing to the subcooled condition of the plate, vapor condenses on it and the condensate liquid flows downwards under the influence of gravity, gradually leading to the formation of a steady liquid film on the surface. Analytical solution for this particular scenario was furnished by Nusselt [2,45] to foretell the film thickness at any location of the plate in terms of the fluid properties and initial and boundary conditions as

$$\delta_f(y) = \left[\frac{4\mu_l\lambda_l(T_s - T_w)y}{gh_{lv}\rho_l(\rho_l - \rho_v)}\right]^{0.25}, \tag{22}$$

where μ_l and λ_l are the viscosity and thermal conductivity of the saturated liquid, h_{lv} is the associated latent heat of condensation, and y is the distance from the leading edge of the plate measured in the direction of gravity. Corresponding local heat transfer coefficient at the surface of the plate can be estimated as $\bar{h}(y) = \lambda_l/\delta(y)$.

The classical theory, however, had several deterrents, such as the nonconsideration of subcooling across the film, which can substantially affect the magnitude of the effective latent heat. A well-accepted amendment was postulated by Rohsenow [2] to reshape the latent heat as

$$h^*_{lv} = h_{lv}\left[1 + 0.68\frac{c_{pl}(T_s - T_w)}{h_{lv}}\right], \tag{23}$$

which has been found to yield very rational predictions, and hence, we have validated our in-house code with the Nusselt's theory after incorporating the above correction.

A schematic representation of the relevant computational domain, along with the imposed boundary conditions, is presented in Fig. 4(a). A rectangular domain having 120×360 lattices is considered, which is initially filled with saturated vapor having $T_s = 0.9\ T_c$. The flat plate is introduced by considering the left vertical boundary of the domain as a no-slip impermeable wall, maintained at $T_w = 0.7\ T_c$. Following Vasyliv *et al.* [30], the bottom boundary is treated as an outflow one with embedded Neumann boundary conditions, while the conditions of the top and right boundaries are detailed in the figure. The vapor film thickness and the local heat transfer coefficient along the wall are compared with the respective analytical solutions in Figs. 4(b) and 4(c) after attaining steady state. Here the film surface is identified as the contour of the average density of both the phases. Excellent degree of conformity with the theoretical solution can be observed for both the parameters, which authenticates the accuracy of the developed solver for condensation on flat surfaces and can now be used to reconnoiter the effect of surface roughness on the droplet nucleation in the next subsection.

C. Formulation of the computational problem

The details of the computational domain under consideration are delineated in this section, along with the adopted initial and boundary conditions to be introduced into the numerical framework. As shown in Fig. 5(a), we have deliberated over a square domain represented by 240×240 lattices, which is initially filled with saturated vapor having $T_{R,\text{sat}} = 0.9$. The bottom edge of the domain simulates a no-slip isothermal wall, whereas the side boundaries are considered to be periodic following Liu and Cheng [23]. The top boundary is assumed to represent the far-field condition, which is ensured by imposing the saturation temperature and

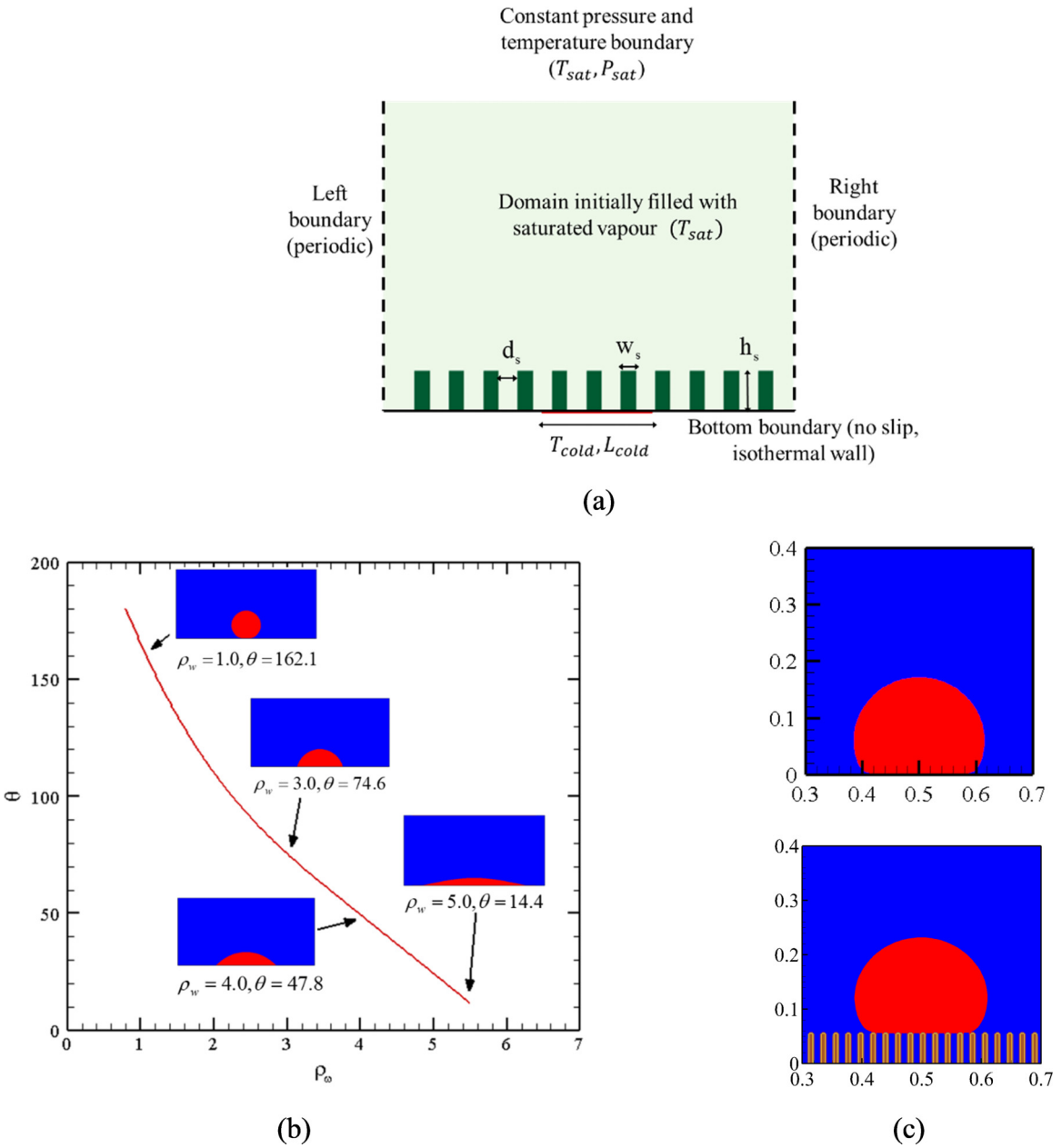

FIG. 5. (a) Schematic representation of the computational domain under consideration, along with the imposed initial and boundary conditions. (b) Variation of the static contact angle (θ) with the false wall density (ρ_w). (c) Static droplet on a plain surface (top figure) with $\rho_w = 1.75$ and on a rough surface (bottom figure) with specific roughness configuration ($w_s = 2$, $h_s = 15$, and $d_s = 3$). Static contact angle for the plain surface continues to be 124°, whereas that enhances to 151° on the rough surface, rendering it to behave as superhydrophobic. Here all dimensions are in lattice unit.

pressure here. All the mentioned conditions are illustrated in the figure as well for ease of comprehension. A cold spot of length $L_{\text{cold}} \equiv 40$ lattice nodes, sustained at the subcooled temperature of $T_{R,\text{cold}}$ ($< T_{R,\text{sat}}$) is placed at the center of the bottom wall, which helps initiating the droplet nucleation. Remainder of the bottom surface is continued to be at $T_{R,\text{sat}}$ only.

Relevant literature in the domain of wettability modulation of rough surface suggest that, with the contemporary manufacturing technology, the highest achievable contact angle of a properly-engineered smooth surface is about 120° [13]. Proper tuning of the morphology of the rough surface is the most feasible option of enhancing the contact angle beyond that ceiling, in an attempt to approach superhydrophobicity. In adherence to various experimental and numerical works [3,14,19,29], we have placed rectangular nanocolumns on the bottom wall, dimensional information for which are available in Fig. 5(a). The effect of gravity is discarded from the mathematical structure ($\mathbf{F}_i^{\text{ext}} \to 0$), as it is expected to be inconsequential at nanoscale [46]. Heat conduction through the solid wall has also been neglected, considering their small dimension in the upward direction, by specifying the

temperature along the entire exterior surface of each of the columns as that of the corresponding poriton of the bottom surface ($T_{R,\mathrm{sat}}$ or $T_{R,\mathrm{cold}}$).

As referred to in Eq. (17), the effective magnitude of surface tension can numerically be modulated by altering the false wall density (ρ_w). With PR-EOS at $T_{R,\mathrm{sat}} = 0.9$, the densities of the saturated liquid and vapor phases are 5.9 and 0.58, respectively. For a choice of ρ_w closer to ρ_l, the contact angle at the three-phase interface is lower, allowing the liquid to wet the surface, whereas with ρ_w approaching ρ_v, the surface advances toward superhyrophobicity. Variation in static contact angle (θ) with ρ_w is presented in Fig. 5(b), which reveals that a change of ρ_w from 1.0 to 5.0 affects a transition in θ from 162.1° to 14.4°. We have maintained at constant magnitude of $\rho_w = 1.75$ throughout the present study, which sets the static contact angle for a droplet on a perfectly smooth surface at $\theta = 124°$, and the same is demonstrated in the top figure of Fig. 5(c). The impact of the presence of nanocolumns on the surface is illustrated in the bottom figure of Fig. 5(c). Here the selected surface structure can be characterized to have column width (w_s) = 2, column height (h_s) = 15, and intercolumn distance (d_s) = 3, with all dimensions being at lattice scale. Clearly the resulting droplet resembles the Cassie state, with a measured contact angle of about 151°, hinting toward the superhydrophobic nature of the solid substrate, despite no change in the fluid-solid combination and hence in the associated force of adhesion. With variations in the characterizing dimensions of the nanocolumns (w_s, h_s, and d_s), it is possible to conceive different magnitudes of the effective contact angle and, therefore, the state of the condensate droplet, which is expected to strongly influence the subsequent hydrodynamics, and the same will be explored from the next subsection onward.

It is pertinent to mention here that all the results presented and discussed within the scope of the current study are ensured to be independent of the choice of number of lattice nodes through a systematic mesh-convergence analysis. Condensation of the Cassie droplet on the surface demonstrated above [Fig. 5(c)] is considered for the same by creating a cold spot on the bottom surface, more on which is deliberated in Sec. III D. Three different lattice configurations, namely 200×200, 240×240, and 280×280, are contemplated, with each producing near-identical droplet shapes, delineated in terms of the thickness of the diffused interface along the vertical centerline, which is measured as the width of the zone over which fluid density changes from liquid level to vapor level. Subsequently, each of the following simulations has been performed using the 240×240 lattice arrangement.

D. Hydrodynamics of the condensate nucleus

Quéré [13] postulated that the roughness topology of a homogeneous rough surface, i.e., the width, height, and spacing of the nanocolumns mounted on the surface, can modify the apparent wettability of the surface itself, coercing alteration in the shape and demeanor of the droplet sitting on it. As demonstrated by Aili *et al.* [47], if the characteristic dimension of the nanostructure is comparable with that of the droplet nucleus, nucleation can get initiated either on the tip of the columns or inside the cavity separating the columns, depending on the energy barrier created by the intrinsic wettability of the surface and geometrical shape of the nucleation site. The final shape of the condensate droplet during condensation on rough surface (Cassie or Wenzel) has been reported through several recent experimental studies [20,46,47], while remaining restricted only to the theoretical appraisal of the nucleation characteristics owing to the lack of proper visualization techniques. One important inference from the available literature [17,47,48] is to identify the change in the free energy during the phase-change process as a primary contributor toward the recognition of the initial nucleation sites. Nucleation is most likely to be triggered at the location having the lowest level of free energy associated with the vapor-liquid transition. As per the classical nucleation theory [47,49], the free energy of heterogeneous nucleation at the three-phase interface is the summation of the three surface energies associated with each pair of phases, which consequently are associated with the continuous creation and extinction of the respective surfaces. For the nanostructured surface with densely packed columns, the solid-liquid interfacial area is greater, necessitating larger energy requirement to form the solid-vapor interface interior to the crevices of the columns, thereby exacerbating the energy barrier. That allows the initiation of droplet nucleation at the tip of the columns, where the energy barrier is weaker because of the smaller solid-liquid interfacial area. Increase in the intercolumn spacing reduces the solid-liquid contact area, consequently lessening the energy barrier in the gaps, and so droplet nucleation on the base surface is more feasible, thereby facilitating the appearance of both the Cassie and Wenzel droplet shapes with variation in the spacing.

One of the primary advantages of the pseudopotential-based LBM is the spontaneous phase separation, without obligating any assumption of initial interface, unlike in conventional CFD-based tools or certain other multiphase LBM models. The adopted PR-EOS controls the coexisting density of both the involved phases. Once the temperature at any lattice node falls below the saturation temperature and sufficient amount of energy is possible to be extracted from the neighborhood of that location, the solver imposes the vapor density value through the EOS, thereby actualizing vapor-to-liquid phase transition. That allows proficient simulation of the local-level microdynamics of the process of droplet nucleation, and we have used that to our advantage to envisage the role of roughness patterns on the droplet state. The simulation setup has already been detailed in Sec. III C. We have maintained a fixed value of $T_{R,\mathrm{cold}} = 0.8T_c$ for the remainder of the work, unless stated otherwise.

The first configuration is selected to have the specifications of $w_s = 3$, $h_s = 15$, and $d_s = 3$ lattice units (lu), and consequent nucleation and growth of a Cassie droplet, nucleating at the top of a nanocolumn, is presented in Fig. 6(a). As explained before, here the arrangement of the structures is too dense to allow phase change inside the cavities, particularly with the entire domain being filled with the vapor phase at $t = 0$. Tiny droplet nuclei are visible at the tip of the adjacent columns around $t = 4200$ lu, which agglomerate into a distinct condensate droplet sitting on the columns around $t = 6000$ lu, with the baseline of the drop having nearly a flat shape. With continuous removal of energy through the cold

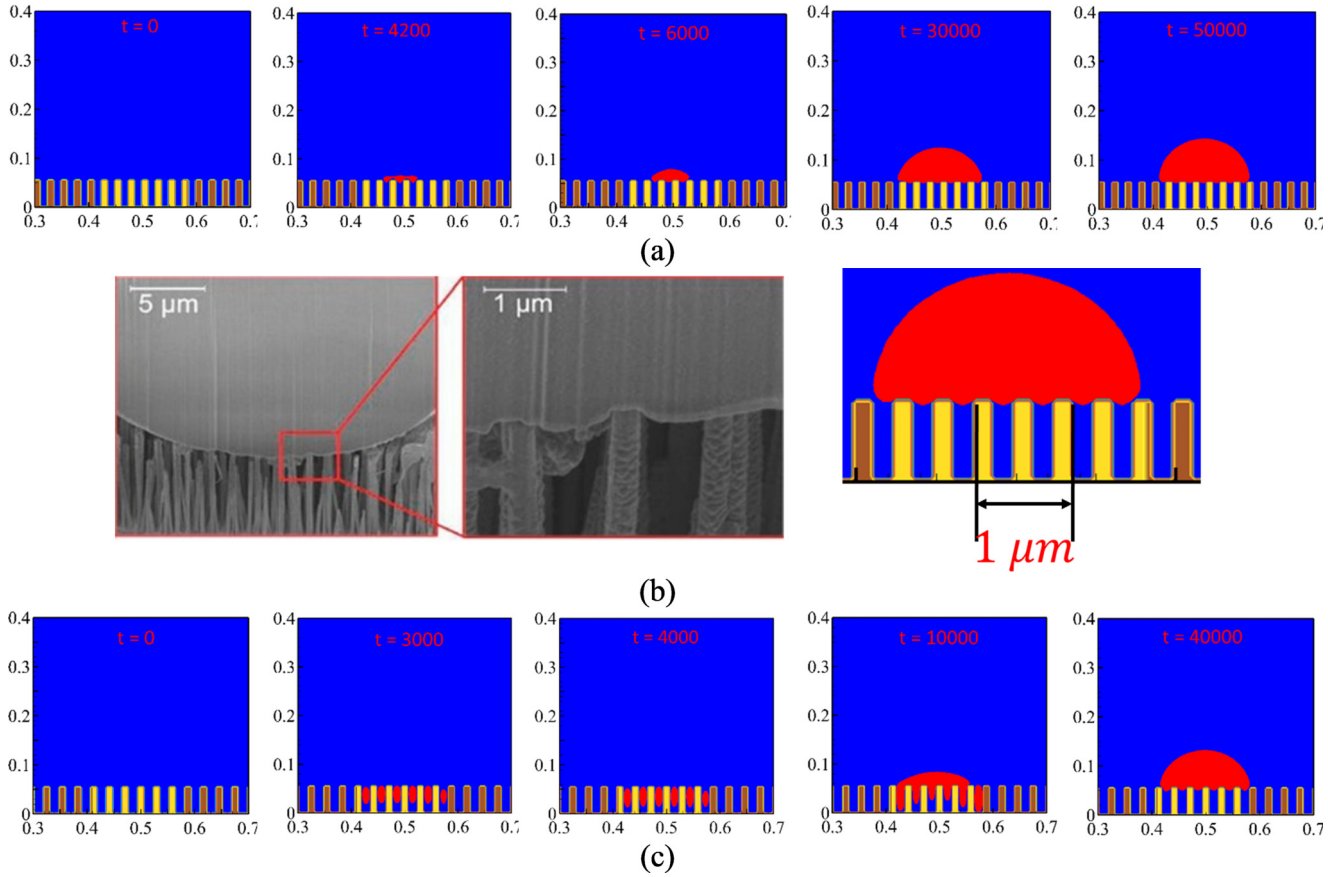

FIG. 6. Cassie droplet. (a) Sequential snapshots in top nucleation mode at different time levels. (b) Qualitative comparison of the present predictions with the experimental results of Rykaczewski *et al.* [20]. (c) Sequential snapshots in side nucleation mode at different time levels. Here all mentioned values are in respective lattice units. The blue and red colors correspond to liquid and vapor phases, respectively, and the cold spot on solid surface is marked in golden color.

spot, the condensate droplet keeps on growing in size, because of the persistent movement of mass across the interface toward the liquid side, and a substantially bigger drop is visible at $t = 50\,000$ lu. It is quite obvious that such a droplet can be removed relatively easily from the rough surface, and therefore a nanostructured surface instigating the top nucleation mode can be viewed to exhibit superhydrophobic nature.

A qualitative comparison is drawn with the experimental pictures reported by Rykaczewski *et al.* [20] in Fig. 6(b) regarding the formation of a Cassie droplet on a solid substrate structured with nanoarrays. One lattice unit of length with present configuration is equivalent to a length scale of 0.5 μm as per the macroscopic system, which allows us to place three nanocolumns over a physical length of 1 μm, as marked in the figure, and it is the same number displayed with the surface used by Rykaczewski *et al.* [20]. We, therefore, have adhered to the same length scale as theirs, which has guided us to the top nucleation mode, establishing the consistency of the numerical prediction with physical microdynamics. Both the experimental and numerical droplets portray very flat nature of the bottom interface, in contact with the columns, which can further be demonstrated following the displacement of the top and bottom interfaces along the vertical center-line, presented in Fig. 7(c). Here the continuous black line corresponds to the upper edge of the interface intersecting that vertical plane, whereas the dotted black one refers to the lower end. Clearly the lower surface always remains in contact with the column, as is unveiled by the straight line. The upper end, however, continually ascends, indicating the growth of the nucleus, as observed earlier in Fig. 6(a).

Increase in the spacing between the columns can allow nucleation on the vertical surfaces of the columns interior to the cavities, initiating the side nucleation mode. It is illustrated in Fig. 6(c), where the surface morphology is specified as $w_s = 3$, $d_s = 4$, and $h_s = 15$ lu, notifying only a single lattice unit of change in the width of the crevices compared to the previous geometry. Here the droplet nucleation starts at a vertical distance of 11 lu from the base surface at $t = 3000$ lu, as shown by the green lines in Fig. 7(c). Initially the droplet grows in both directions, with the bottom interface moving toward the base. Around $t = 4000$ lu, the upper interface reaches the tip of the column, which restricts any further downward displacement of the bottom edge of the interface. The lower interface, which is yet to touch the base, in fact, starts climbing upward after a short while, until it arrives at the tip of the column and stays there, impressing a Cassie state of the nucleus from that instant onward. Zhang *et al.* [14] attributed such ascension of the condensate droplet, despite the side nucleation, to the Laplace pressure difference. As the upper surfaces of the individual nuclei merge with each other

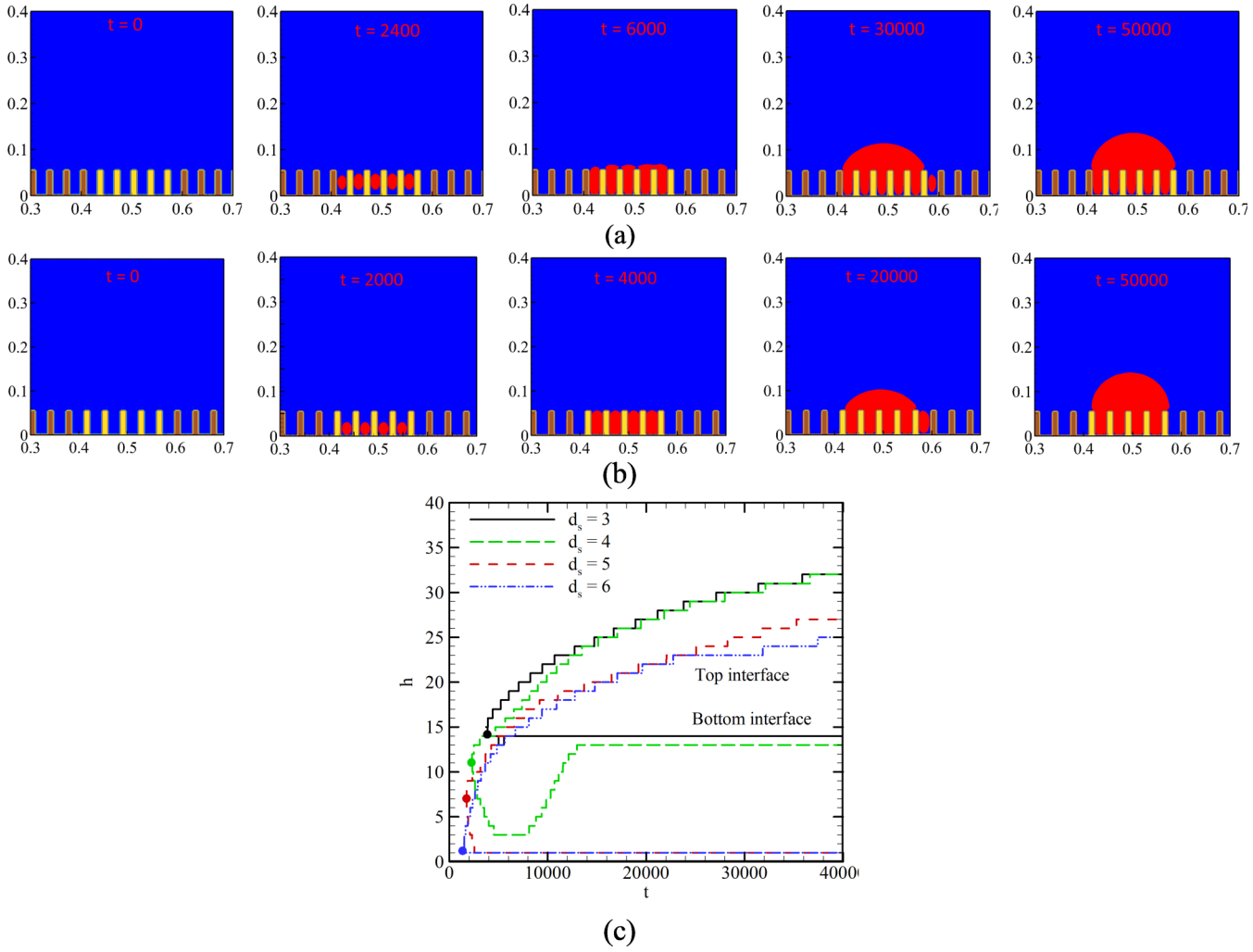

FIG. 7. Wenzel droplet. (a) Sequential snapshots in side nucleation mode at different time levels. (b) Sequential snapshots in bottom nucleation mode at different time levels. (c) Movement of the top and bottom interfaces of the condensate droplet along the vertical centerline for all the four cases. Here all mentioned values are in respective lattice units. The blue and red colors correspond to liquid and vapor phases, respectively, and the cold spot on solid surface is marked in golden color.

to form a bigger one, there is reduction in the local radius of curvature in that part of the interface. Now the pressure differential across the interface being inversely proportional to the radius and the ambient pressure being a constant one, there will be a decline in local pressure in the upper section of the droplet. The magnitude in the lower part, however, remains unchanged, resulting in an upward thrust capable enough of dragging each of the tiny droplets out of their respective cavities, and allowing the formation of a single Cassie droplet settled on the tip of the nanostructures. From both Figs. 6(c) and 7(c), we can ascertain that the extraction of the droplets starts around $t = 8110$ lu and completes approximately at $t = 12980$ lu. A growing Cassie droplet is clearly visible at $t = 40\,000$ lu, indicating the attainment of superhydrophobicity even with side nucleation.

A discernible change in the state of the droplet nucleus can be realized with another lattice unit of increase in the width of the cavities ($d_s = 5$ lu). The initiation of phase change still continues to be in side nucleation mode, albeit starting at a vertical position of about 7 lu, lower than the previous case, as can be ascertained from the red lines plotted in Fig. 7(c). Such a change in positioning can possibly be attributed to the competition between the prevailing energy barrier and heat transmission from the cold wall. As a consequence, the bottom interface touches the base surface at $t = 2550$ lu, with the upper edge still languishing about 5 lu below the tip of the columns, thereby not allowing any coalescence of the individual nuclei. Hence, there is no unbalanced Laplace pressure to lift the droplets and the same adheres to the base, as well as the vertical walls of the columns, owing to the adhesive forces [Fig. 7(a)]. That is also evident from the displacement of the lower part of the interface, which, after a short initial time span, always sticks to the location $h = 0$. The sizes of the individual droplets get augmented with time because of the transformation of vapor to liquid coming in contact with the cold column walls, eventually stretching out of the cavities around $t = 6000$ lu and merging with each other to form a single droplet. This, however, always encompasses the columns attached to the cold spot and also remains in contact with the base surface, which is the precise characteristics of the Wenzel state. It leads to the filmwise condensation, in contrast to the dropwise condensation evident with the Cassie

state, therefore tending more to the hydrophilic nature of the surface despite the presence of the nanostructures.

With any further enhancement in the intercolumn spacing, nucleation may get initiated from the base surface itself. One such scenario is presented through the snapshots in Fig. 7(b) for $d_s = 6$ lu and also by the temporal displacement of the two representative points on the interface in Fig. 7(c) (blue line). Lower surface of the droplet never leaves the base since nucleation, whereas the upper edge creeps out of the cavity after $t = 4000$ lu, gradually developing into a Wenzel drop and consequent condensate film on the surface. Such filmwise condensation, generally, is not favored in commercial heat transfer appliances, as it deteriorates the rate of energy transmission owing to the loss of the contact between the subcooled surface and saturated vapor. The superiority of dropwise condensation in this precise context, because of the prompt removal of the condensate drop and continuity of the latent heat transfer, is well documented in the literature [6,7,17,50], accentuating the role of the nanocolumns in resolving the nature of condensation.

E. Interfacial mass and energy interactions

In at attempt to acquire precise perception about the rate of interfacial interactions with either states of droplet nucleation, we analyze the rate of surface heat transfer at the cold spot ($q = -\lambda A_{\text{cold}} \frac{\partial T}{\partial n}$) and instantaneous mass of condensate ($\dot{m}_l$) with time for each of four cases explored in the previous Sec. III D. Here λ is the thermal conductivity of the fluid in contact with the cold surface and $\hat{n}$ is the direction normal to the same plane. Li *et al.* [29] discussed the trend regarding the same parameters during condensation on rough surfaces with variable wettability and identical geometric morphology. Adhering to their conjecture and also following the microdynamics of condensation at the cold spot observed during the present study, we can identify four distinct stages of heat transfer.

(i) As the temperature of initially saturated vapor starts decreasing with it losing energy to the subcooled solid, the consequent temperature differential ΔT reduces. Prior to the initiation of phase transition, only sensible mode of heat transfer is possible, and that being proportional to ΔT, the overall rate of heat transfer falls over a brief period.

(ii) Once sufficient level of vapor subcooling has been achieved, condensation is instigated, and latent mode of heat transfer is materialized, leading to a sharp rise in the rate of energy interaction. Small amount of sensible heat transfer also commences to the newly appearing liquid phase.

(iii) As the droplet grows in size, the cold spot increasingly gets covered by liquid. The consequent temperature differential between the surface and the adjacent fluid is much lower now, which hinders energy transmission, causing a consequent decline in q. The proportion of latent mode in overall heat transfer diminishes rapidly with time.

(Iv) Eventually the steady-state scenario is achieved, with the cold spot being fully covered by liquid, and heat absorption from the vapor to the substrate is possible only through the liquid layer, which offers reasonably high thermal resistance.

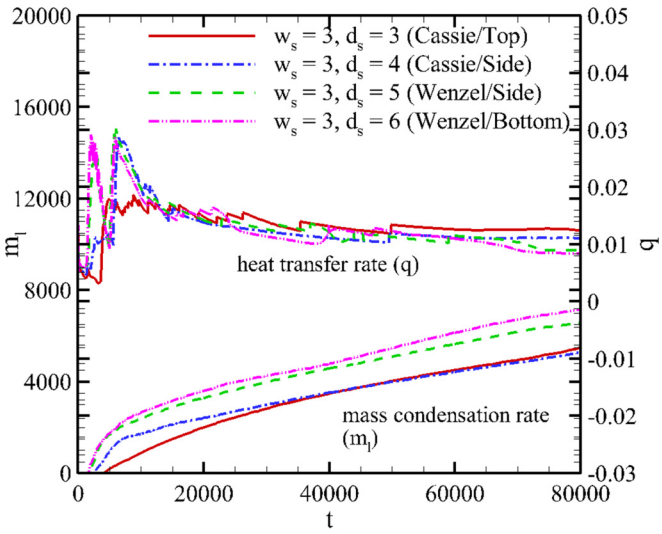

FIG. 8. Temporal variations in heat transfer rate at the solid surface (q) and accumulated mass of the condensate (m_l) for all the cases presented in Figs. 6 and 7, with different intercolumn spacing (d_s) and identical dimensions of individual columns ($w_s = 3$ and $h_s = 15$). Here all mentioned values are in respective lattice units.

A similar nature of transient progression can be found in Fig. 8 for the present study as well. The rate of heat transfer decreases over a short time span until the inception of nucleation, characterized by a rapid upsurge to attain a maxima, and then falls continuously with a moderate gradient. The magnitude of q_{max} is quite similar in all the cases apart from the top nucleation mode, where the active contact area is significantly smaller than the side or bottom nucleation cases. In fact, Cassie droplet in top nucleation mode does not exhibit any sharp decline in q beyond the peak. Interestingly, two peaks can be observed in both the modes of Wenzel state. While the appearance of the very first liquid nucleus corresponds to the first peak, the second peak possibly is a consequence of the activation of greater contact area with time. The steady-state magnitude of q with Cassie drop in top nucleation mode is slightly higher than the rest, as a consequence of the lesser thickness of the liquid layer. The rate of condensation follows the profile of q. It is significantly high during the initial phases of nucleation and droplet growth, as direct latent energy absorption is possible at the cold spot. Quéré [13] pointed out that the increment in the intercolumn spacing lowers the apparent wettability of the solid substrate, as explained earlier using the concept of Laplace pressure. The energy barrier associated with the vapor-to-liquid phase transition is weaker with reduced wettability and, hence, favorable for condensation, thereby allowing earlier droplet nucleation and greater rate of mass condensation with declining hydrophobicity of the cold surface. That argument is consistent with our observation, as d_s is varied from three to six lattice units in Fig. 8. The Wenzel state of nucleation is found to be associated with early commencement of phase transformation, as well as greater mass of condensate accumulation with time, compared to the Cassie state. The filmwise condensation is classically known to yield considerably lower rate of heat transfer than the dropwise mode [6,8].

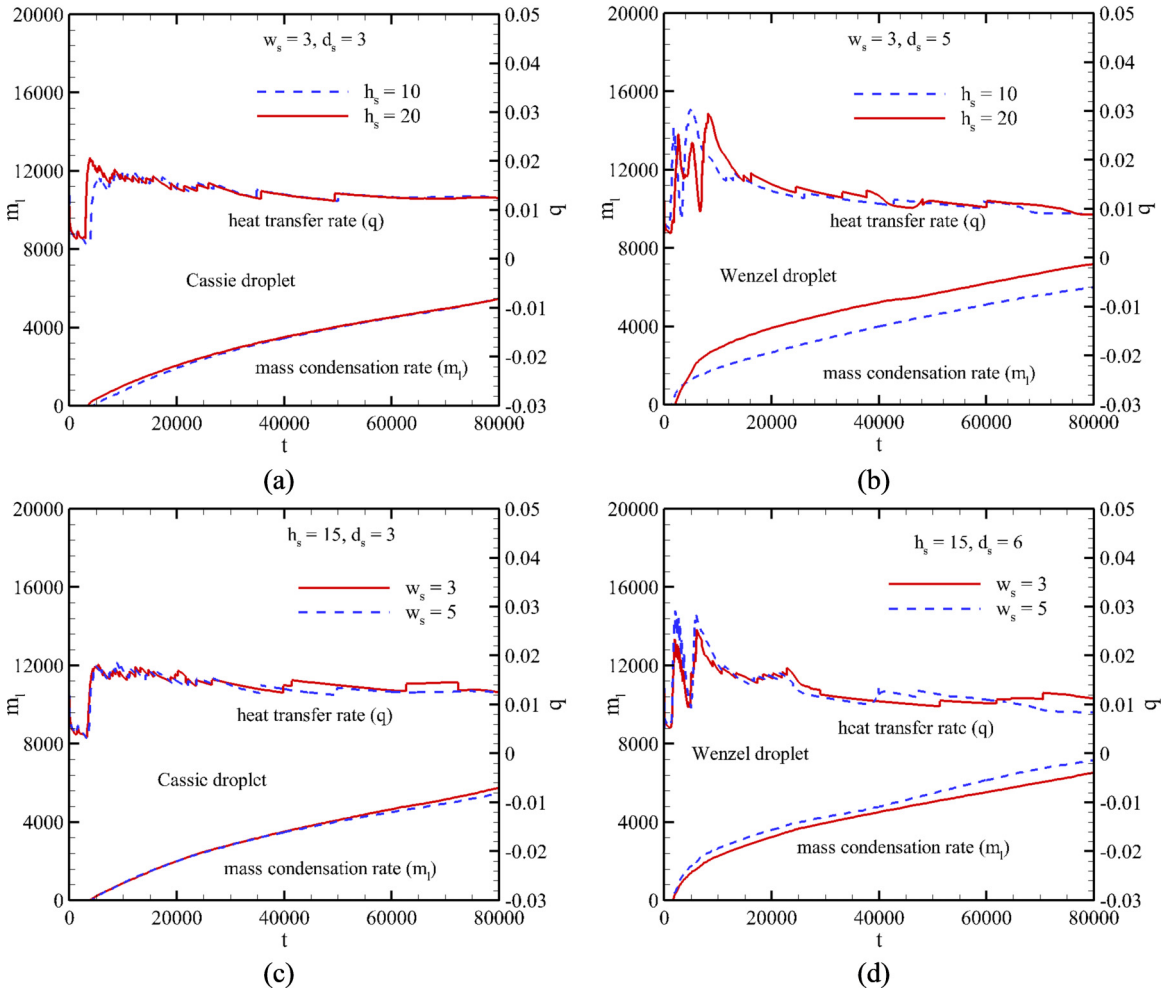

FIG. 9. Temporal variations in heat transfer rate (q) and mass of condensate (m_l): Effect of column height (h_s) on (a) a Cassie droplet ($d_s = 3$) and (b) a Wenzel droplet ($d_s = 5$); effect of column width (w_s) on (c) a Cassie droplet ($d_s = 3$) and (d) a Wenzel droplet ($d_s = 6$). Here all mentioned values are in respective lattice units.

All the discussion to this point has revolved around the role of intercolumn spacing on the nucleation characteristics. The repercussion of change in other relevant dimensions of the nanostructures is not that substantial, primarily because they do not significantly impact the apparent wettability of the surface. Several such cases are demonstrated in Fig. 9, where the ones in the top row illustrate the impact of column height (h_s), while the bottom ones represent the implications of change in width (w_s). The height (h_s) clearly has inconsequential impression on the rate of interactions for a Cassie droplet ($d_s = 3$ lu). The rate of mass condensation for a Wenzel droplet, however, is substantially enhanced with rise in h_s [Fig. 9(b)]. The rationale lies with the accretion in the area available for heat extraction. While the Cassie droplet is in contact only with the tip of the column, which remains unchanged with any alteration in the height, the Wenzel droplet wets the base surface, as well as the side walls of the columns. With $h_s = 20$ lu, it is possible to offer wider cold spot to the saturated vapor, emanating noticeably higher m_l.

The effect of the column width (w_s) is even less recognizable for both the droplet states. The rate of condensation is slightly lesser for the Wenzel drop with wider columns, as the available base area is lesser.

F. Nucleation time

As the apparent wettability of a nanostructured surface is modulated by adjusting the dimensions of the nanoarray, the time required for nucleation (t_n) is also attuned accordingly. Here the nucleation time has been numerically estimated as the time required for the liquid phase to occupy 10 lattice cells since the very inception of simulation. Hydrophilic surface has a greater affinity to the liquid phase, providing additional impetus toward condensation, and therefore, any change leading toward hydrophilicity helps in early nucleation. The same can be affirmed following the trends evident in Fig. 10. Substantially greater time is required to initiate the Cassie droplets, particularly in the top nucleation mode, as the area consequent to heat transfer is the smallest among all the orientations considered here. Appearance of liquid phase is almost instantaneous in the Wenzel state, again owing to the availability of wider cold surface. Time requirement increases with the column height to a certain level, beyond which it becomes

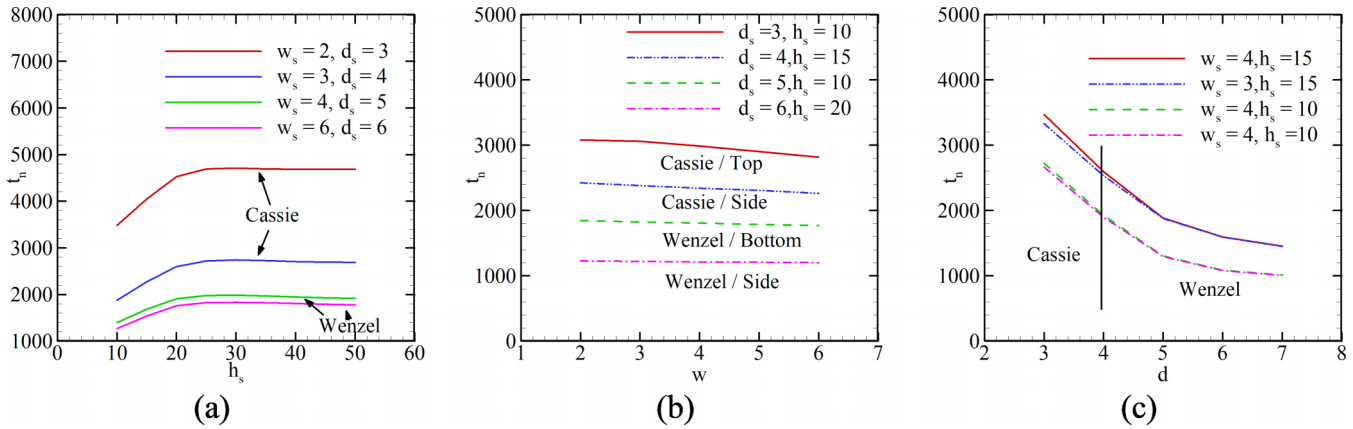

FIG. 10. Variation in nucleation time (t_n) with (a) column height (h_s), (b) column width (w_s), and (c) intercolumn spacing (d_s). Here all mentioned values are in respective lattice units.

invariant for any kinds of nucleation [Fig. 10(a)]. Nucleation time is found to be decreasing with column width (w_s) for the Cassie droplet in top nucleation mode from Fig. 10(b). As the Cassie drop engages only with the tip of the column for energy interaction, any increment in w_s provides greater contact area between the solid and vapor and hence an early incipience of condensation. For side or bottom nucleation modes, however, there is hardly any change in t_n with w_s for very obvious reasons.

An interesting pattern can be observed from Fig. 10(c) that shows the effect of the intercolumn spacing (d_s). As detailed in the previous sections, a bigger gap between the neighboring columns diminishes the hydrophobic character, promoting the transformation from the Cassie to Wenzel state. Remaining consistent with the tendency of the Wenzel drops to nucleate promptly, a steep fall in the nucleation time can clearly be identified for any combination of height and width. Beyond a certain magnitude of d_s, though, the profiles for any types of nucleation become near horizontal, as the columns are now too far apart from each other to inflict the impact of the nanoarray.

G. Phase diagram

In many industrial applications, it is generally preferable to have droplet condensation to facilitate higher rate of heat transfer and also easier removal of the condensate. Therefore, based on the discussions to this point, it can be inferred that an array of densely packed taller and slimmer columns is desirable to ensure Cassie droplet in top nucleation mode and so a superhydrophobic substrate. Certain combinations of intermediate spacing and height can lead to side nucleation, raising the possibility of both Cassie and Wenzel nucleation, depending on the positioning of the lower interface of the droplet at the instant of the upper interface peeping out of the cavity, while a large intercolumn spacing always actuates bottom nucleation. In an attempt to accomplish complete cognizance about the possible modes of nucleation for any specific surface morphology, all the explored combinations are summarized in a pair of phase diagrams in Fig. 11. When the columns are very closely spaced ($d_s \lessapprox 3$ lu), phase transition is always happening through Cassie drops in top nucleation mode. With increase in the spacing beyond that, however, the side nucleation is prompted, continuing to yield

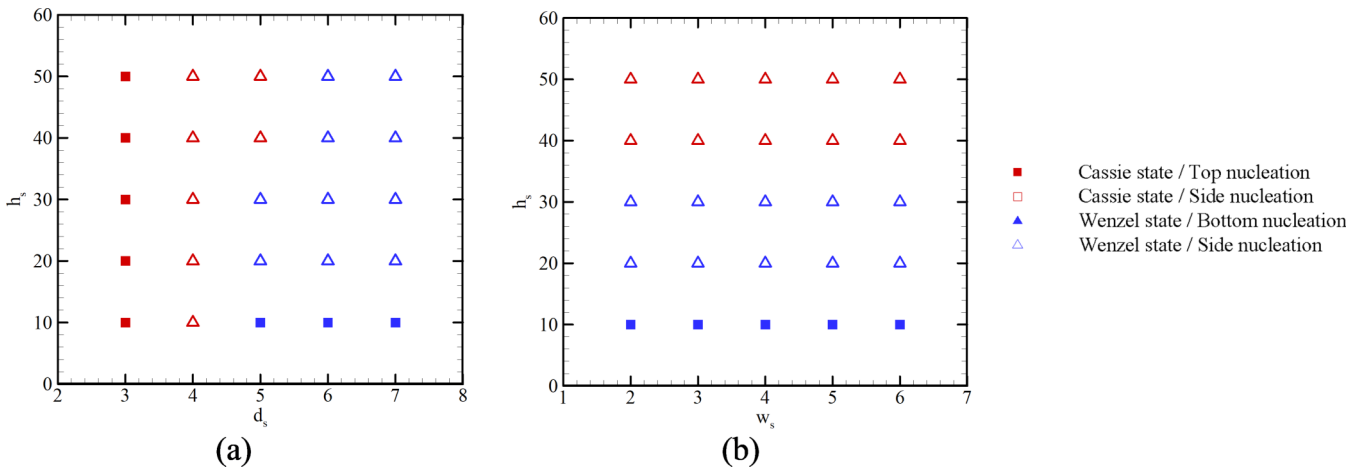

FIG. 11. Phase diagrams encompassing all four modes of droplet nucleation on a nanostructured surface on (a) the $h_s - d_s$ plane with $w_s = 4$ and (b) the $h_s - w_s$ plane with $d_s = 5$. Here all mentioned values are in respective lattice units.

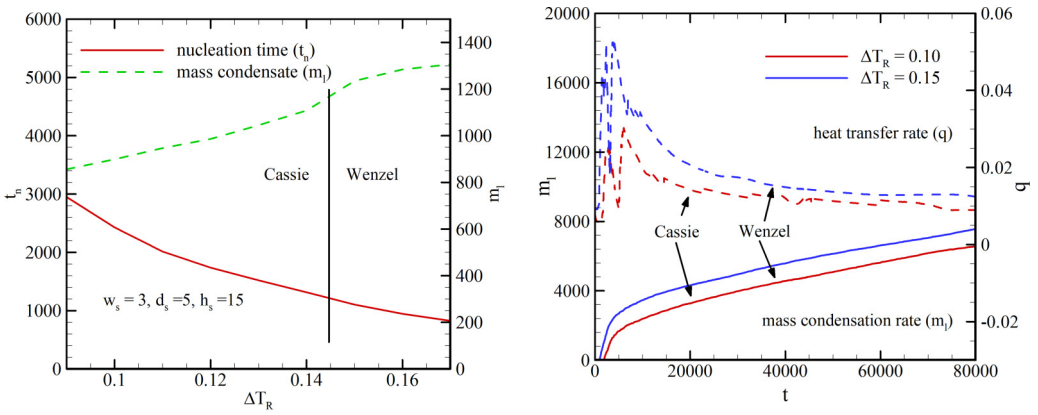

FIG. 12. (a) Effect of the degree of subcooling ($\Delta T_R = T_{R,\text{sat}} - T_{R,\text{cold}}$) on the nucleation time and total mass of condensate accumulated to $t = 50\,000$, with the droplet changing from the Cassie to Wenzel state for high ΔT_R. (b) Temporal variations in heat transfer rate (q) and mass of condensate (m_l) for two different cold spot temperatures. Here all mentioned values are in respective lattice units.

Cassie drops over a short range. An interesting pattern can be noted following a vertical line drawn at $d_s = 5$ lu. Such a spacing leads to Wenzel drops in the bottom nucleation mode for shorter columns ($h_s \approx 10$ lu) and in the side nucleation mode for intermediate heights. When the columns are reasonably tall ($h_s > 40$ lu), the process of condensation reverts back to the Cassie drops with side nucleation, as the lower interface of a growing nucleus is not able to make to the base surface. With further increase in the spacing, only Wenzel drops, instigating filmwise condensation, is possible, with the mode of bottom or side nucleation being determined by the column heights. As already recognized in Sec. III E, the width of the column has an inconsequential role in determining either the nature of nucleation or the rates of interactions. The same can be reinforced by developing similar phase diagrams for other column widths to identify no perceptible change in the conclusions.

H. Effect of cold spot temperature

One of the prime novelty of the present work, in retrospect to the existing LBM studies on condensation [14,28], is the consideration of thermal nonequilibrium within the condensate layer. A selected section of the base surface, one-sixth of the total length, is imposed with lower temperature, while maintaining the remainder at the saturation value, thereby creating a cold spot and, hence, a stimulus for energy interaction between the saturated vapor and the surface structures. Each of the earlier results corresponds to a low temperature of $T_{R,\text{cold}} = 0.8$ lu, inflicting a degree of subcooling of $\Delta T_R = T_{R,\text{sat}} - T_{R,\text{cold}} = 0.1$ lu. To ascertain the influence of this temperature, $T_{R,\text{cold}}$ has been regulated over the range of 0.81 to 0.73 lu, subsequently administering ΔT_R of 0.09 to 0.17 lu, respectively, and associated observations are illustrated in Fig. 12.

Any lowering in the temperature of the cold spot renders greater potential for absorption of energy from the vapor phase and therefore promotes condensation. Consequently, the amount of time required for nucleation (t_n) continually reduces with rise in ΔT_R, while the mass of condensate accumulated over a certain time span steadily increases, as can be endorsed from Fig. 12(a). Another conspicuous phenomenon to note is the transition from the Cassie to Wenzel state for $\Delta T_R \geqslant 0.15$ lu. Our choice of the nanostructured surface for the present set of simulations can be defined with $w_s = 3$, $h_s = 15$, and $d_s = 4$ lu, which yielded Cassie droplet in side nucleation mode for $T_{R,\text{cold}} = 0.8$ lu, as discussed earlier. For such levels of ΔT_R, the nucleus is forced to climb along the columns toward the tip under the action of the unbalance Laplace pressure. For lower $T_{R,\text{cold}}$, though, the rate of generation of liquid is significantly faster, allowing the initial droplet nucleus to experience accelerated growth and fill the cavity up in much lesser time. When ΔT_R swells beyond 0.15 lu, the lower surface of the interface is able to contact the base surface before the top can creep out of the cavities. There is no creation of unbalance in Laplace force as a consequence, facilitating the transition to the Wenzel state, with the droplet adhering to the base surface and side walls of the columnar structures. There is also a change in the amount of condensate mass, with no appreciable deviation in the profile of the nucleation time.

The rates of energy and mass interactions are compared in Fig. 12(b) for two different temperatures of the cold spot. As expected, both are higher for the cooler surface with $\Delta T_R = 0.15$ lu, which is associated with the Wenzel state. Noticeably early initiation of the phase transition can be observed for this case, along with substantially higher magnitude of the peak heat flux and much steeper rise in the condensate accumulation rate. It can, therefore, be concluded that the surface temperature can also effectuate critical evolution in the microdynamics of the droplet nucleus, as well as the rate of interfacial interactions, along with the nanostructures. It is preferable to perpetuate a controlled level of subcooling at the cold spot to ensure the superhydrophobic nature.

IV. CONCLUSIONS

In the present study, we have delved into the intriguing scenario of condensation on nanostructured surfaces, where the nature of nucleation and associated thermalhydraulics are

closely regulated by the specifications of the surface architecture. While systematic experiments have greatly contributed in comprehending corresponding visual nature of droplet nucleus, detailed numerical analyses are necessary to unearth crucial information about the local transport characteristics, and the mesoscopic framework of LBM has been employed here. We have adopted an MRT-based LBM structure, in collaboration with the pseudopotential model, to envisage the role of the dimensions of the nanocolumns mounted on the bottom surface of a rectangular domain. The computational domain is initially assumed to be filled up with saturated vapor and a cold spot has been imposed at the center of the base surface to facilitate phase transition.

The most important observation is the attainment of superhydrophobic condition for certain combination to the column dimensions and intercolumn spacing, with the later parameter being earmarked as the most influential one, despite the static contact angle with the selected fluid-solid pair on a smooth surface being only around 124°. Both the Cassie and Wenzel states of nucleus are possible to be achieved, with sequential appearance of the top, side, and bottom modes of nucleation with gradual widening of the intercolumn gaps, primarily owing to the consequent modulation in the apparent wettability of the cold spot. Superhydrophobicity is associated with the Cassie state, which allows the droplet to sit at the tip of the columns, even during side nucleation, thereby expediting easy removal of liquid. Influences of both the height and width of the columns are found to be near-inconsequential on the overall characteristics, as neither sufficiently affect the apparent wettability and associated imbalance in Laplace pressure. Reduction in the temperature of the cold spot also promotes early condensation, with a Cassie-to-Wenzel transition for greater degree of subcooling.

Four distinct stages of heat transfer can be recognized, with each according a different proportion of sensible and latent energy transmission to varying fluid phases. The Wenzel state is found to demonstrate early nucleation and larger amount of condensation, with particularly steep gradient of condensate formation during the early stages of the process. It also displays greater surface heat flux, uniquely characterized by two peaks of near-identical magnitude. The Cassie state with side nucleation can attain a similar level of maxima in heat flux, albeit at a noticeably later instant, leading to a lower time-average value. q for Cassie droplet in top nucleation mode, however, is consistently the inferior one, specifically during the first three stages of energy interactions, because of the limited contact area. All the four condensation scenarios are summarized through couple of phase diagrams, which aid easy identification of the mode of nucleation from the knowledge of the surface topology, and subsequent characterization of the local thermalhydraulics of the phase-change process.

ACKNOWLEDGMENTS

All the computations reported here are carried out in the PARAM-ISHAN cluster, a 162-node, 250 tfps hybrid high-performance computing facility at IIT Guwahati. D.N.B. acknowledges the funding supports received from CAS President's International Fellowship for Visiting Scientists, China (No. 2020VEB0006), and Science and Engineering Research Board (SERB), India (No. EMR/2017/000277), 2018. L.C. has been supported by the National Natural Science Foundation of China (No. 52076207) and the Key Research Program of the CAS Innovation Academy for Light-duty Gas Turbine (CXYJJ21-ZD-01).

[1] J. G. Collier and J. R. Thome, *Convective Boiling and Condensation*, 3rd ed. (Clarendon Press, London, 1994).
[2] S. M. Ghiaasiaan, *Two-Phase Flow, Boiling, and Condensation: In Conventional and Miniature Systems* (Cambridge University Press, Cambridge, UK, 2007).
[3] Y. Li and W. Ren, Langmuir **30**, 9567 (2014).
[4] H. Lee, C. R. Kharangate, N. Mascarenhas, I. Park, and I. Mudawar, Int. J. Heat Mass Transf. **85**, 865 (2015).
[5] E. Da Riva and D. Del Col, Micrograv. Sci. Technol. **23**, 87 (2011).
[6] J. Rose, Proc. Inst. Mech. Eng. A: J. Power Energy **216**, 115 (2002).
[7] C. R. Kharangate and I. Mudawar, Int. J. Heat Mass Transf. **108**, 1164 (2017).
[8] S. Vemuri and K. Kim, Int. J. Heat Mass Transf. **49**, 649 (2006).
[9] K.-C. Park, H. J. Choi, C.-H. Chang, R. E. Cohen, G. H. McKinley, and G. Barbastathis, ACS Nano **6**, 3789 (2012).
[10] P. Guo, Y. Zheng, M. Wen, C. Song, Y. Lin, and L. Jiang, Adv. Mater. **24**, 2642 (2012).
[11] R. Wen, S. Xu, X. Ma, Y.-C. Lee, and R. Yang, Joule **2**, 269 (2018).
[12] T. M. Thomas and P. Sinha Mahapatra, Langmuir **37**, 12767 (2021).
[13] D. Quéré, Annu. Rev. Mater. Res. **38**, 71 (2008).
[14] Q. Zhang, D. Sun, Y. Zhang, and M. Zhu, Langmuir **30**, 12559 (2014).
[15] Y. Jung and B. Bhushan, J. Microsc. **229**, 127 (2008).
[16] B. Shin, K.-R. Lee, M.-W. Moon, and H.-Y. Kim, Soft Matter **8**, 1817 (2012).
[17] A. Starostin, V. Valtsifer, Z. Barkay, I. Legchenkova, V. Danchuk, and E. Bormashenko, Appl. Surf. Sci. **444**, 604 (2018).
[18] J. B. Boreyko and C.-H. Chen, Phys. Rev. Lett. **103**, 174502 (2009).
[19] R. Narhe and D. Beysens, Langmuir **23**, 6486 (2007).
[20] K. Rykaczewski, T. Landin, M. L. Walker, J. H. J. Scott, and K. K. Varanasi, ACS Nano **6**, 9326 (2012).
[21] R. Enright, N. Miljkovic, J. L. Alvarado, K. Kim, and J. W. Rose, Nanosc. Microsc. Thermophys. Eng. **18**, 223 (2014).
[22] T. Krüger, H. Kusumaatmaja, A. Kuzmin, O. Shardt, G. Silva, and E. Viggen, *The Lattice Boltzmann Method: Principles and Practice* (Springer, Berlin, 2016).
[23] X. Liu and P. Cheng, Int. J. Heat Mass Transf. **64**, 1041 (2013).
[24] X. Liu and P. Cheng, Int. J. Heat Mass Transf. **62**, 507 (2013).

[25] X. Li, J. Zhao, and P. Cheng, Int. J. Heat Mass Transf. **114**, 628 (2017).
[26] X. Li and P. Cheng, Int. J. Heat Mass Transf. **110**, 710 (2017).
[27] S. Zheng, F. Eimann, T. Fieback, G. Xie, and U. Gross, Appl. Therm. Eng. **145**, 590 (2018).
[28] X. Fu, Z. Yao, and P. Hao, Langmuir **30**, 14048 (2014).
[29] M. Li, C. Huber, W. Tao, and J. Wei, Int. J. Heat Mass Transf. **131**, 96 (2019).
[30] Y. Vasyliv, D. Lee, T. Tower, R. Ng, V. Polashock, and A. Alexeev, Int. J. Heat Mass Transf. **136**, 196 (2019).
[31] A. Montessori, M. Lauricella, N. Tirelli, and S. Succi, J. Fluid Mech. **872**, 327 (2019).
[32] A. Montessori, M. Lauricella, A. Tiribocchi, F. Bonaccorso, and S. Succi, J. Chem. Phys. **152**, 144101 (2020).
[33] A. Montessori, A. Tiribocchi, M. Lauricella, and S. Succi, J. Comput. Sci. **44**, 101160 (2020).
[34] A. Montessori, P. Prestininzi, M. La Rocca, and S. Succi, Phys. Fluids **29**, 092103 (2017).
[35] X. Shan and H. Chen, Phys. Rev. E **47**, 1815 (1993).
[36] Q. Li, K. H. Luo, and X. J. Li, Phys. Rev. E **87**, 053301 (2013).
[37] W.-Z. Fang, L. Chen, Q.-J. Kang, and W.-Q. Tao, Int. J. Therm. Sci. **114**, 172 (2017).
[38] Q. Li, K. H. Luo, and X. J. Li, Phys. Rev. E **86**, 016709 (2012).
[39] X. Shan and H. Chen, Phys. Rev. E **49**, 2941 (1994).
[40] X. Shan, Phys. Rev. E **77**, 066702 (2008).
[41] P. Yuan and L. Schaefer, Phys. Fluids **18**, 042101 (2006).
[42] S. Gong and P. Cheng, Comput. Fluids **53**, 93 (2012).
[43] R. Benzi, L. Biferale, M. Sbragaglia, S. Succi, and F. Toschi, Phys. Rev. E **74**, 021509 (2006).
[44] S. Gong and P. Cheng, Int. J. Heat Mass Transf. **55**, 4923 (2012).
[45] T. L. Bergman, F. P. Incropera, D. P. DeWitt, and A. S. Lavine, *Fundamentals of Heat and Mass Transfer*, 7th ed. (John Wiley & Sons, New York, 2011).
[46] C. Lv, P. Hao, X. Zhang, and F. He, ACS Nano **9**, 12311 (2015).
[47] A. Aili, Q. Ge, and T. Zhang, J. Heat Transf. **139**, 112401(2017).
[48] A. S. Abyzov, J. W. Schmelzer, and L. N. Davydov, J. Chem. Phys. **147**, 214705 (2017).
[49] R. David and A. W. Neumann, Colloids Surf., A **425**, 51 (2013).
[50] B. S. Sikarwar, K. Muralidhar, and S. Khandekar, Interfacial Phenom. Heat Transf. **1**, 339 (2013).